Nonlinear dynamical tunneling of optical whispering gallery modes in the presence of a Kerr nonlinearity

Jeong-Bo Shim,[1,2] Peter Schlagheck,[1] Martina Hentschel,[3] and Jan Wiersig[2]
[1]*Département de Physique, University of Liège, 4000 Liège, Belgium*
[2]*Institut für Theoretische Physik, Otto-von-Guericke-Universität Magdeburg, D-39016 Magdeburg, Germany*
[3]*Institut für Physik, Technische Universität Illmenau, D-98693 Illmenau, Germany*
(Received 16 December 2015; published 28 November 2016)

The effect of a Kerr nonlinearity on dynamical tunneling is studied, using coupled whispering gallery modes in an optical microcavity. The model system that we have chosen is the "add-drop filter," which is comprised of an optical microcavity and two waveguides coupled to the cavity. Due to the evanescent fields scattering on the waveguide, the whispering gallery modes in the microcavity form doublets, which manifest themselves as splittings in the spectrum. As these doublets can be regarded as a spectral feature of dynamical tunneling between two different dynamical states with a spatial overlap, the effect of a Kerr nonlinearity on the doublets is numerically investigated in the more general context of the relationship between cubic nonlinearity and dynamical tunneling. Within the numerical realization of the model system, it is observed that the doublets show a bistable transition in their transmission curve as the Kerr nonlinearity in the cavity is increased. At the same time, one rotational mode becomes dominant over the other one in the transmission, since the two states in the doublet have uneven linewidths. By using coupled-mode theory, the underlying mode dynamics of the phenomena is theoretically modeled and clarified.

DOI: 10.1103/PhysRevA.94.053849

I. INTRODUCTION

A whispering gallery mode (WGM) in a microcavity is recognized for its easy experimental realization and high cavity quality factor (Q factor). Using such properties of WGMs, high intensity can be easily induced in a micrometer-scale optics, and the induced high intensity allows for $\chi^{(3)}$-nonlinear optical effects [1]. Recently, the nonlinear optical effect of microcavities has demonstrated various applications. In particular, the optical frequency comb generation, which is enabled by the $\chi^{(3)}$-nonlinear optical effect of a microcavity, has attracted researchers' interest [2,3] because of its wide range of applications.

It is thus interesting to understand other phenomena related to the $\chi^{(3)}$-nonlinearity, which can occur in a microcavity experiment. The Kerr effect is a manifestation of the $\chi^{(3)}$-nonlinear effect, by which the refractive index is tuned proportional to the squared value of the electric field. A pronounced effect of the Kerr nonlinearity is the bistability of an optical resonant mode. If a resonant mode is excited in an optical resonator filled with a Kerr-nonlinear material, every point on the resonance profile sees a different refractive index due to the enhanced intensity. This difference in the refractive index results in the shift of the resonant frequency. If the shift surpasses a certain threshold, the whole resonance profile appears to lean to one side, and a part of it becomes bistable, i.e., two stable amplitudes correspond to a given driving frequency [1]. This process is called "bistable transition."

A microcavity filled with a Kerr-nonlinear material can exhibit bistability and the bistable transition of a WGM. Up to now, the bistability of a WGM has been studied for various applications such as optical switches or filters [4,5]. In this work, however, we are going to focus on another aspect of the Kerr effect in a microcavity, namely its relationship with dynamical tunneling.

"Dynamical tunneling" refers to a transition of dynamical states in quantum and wave mechanics that is forbidden in classical ray dynamics [6,7]. It hereby extends the usual concept of quantum (or wave) mechanical tunneling across potential barriers in configuration space to the more general phase-space domains. In the past decade, the phenomena relevant to the dynamical tunneling have been actively explored, using various systems including cold-atom systems and WGMs [8–13].

As a solution of Maxwell's equations, a WGM has an intrinsic time-reversal symmetry, which manifests itself in two counterpropagating waves. Owing to the high Q factor again, the degeneracy of a WGM can be lifted by a small perturbation, such as Rayleigh scattering [14,15]. The doublet of a WGM can be interpreted as a state resulting from tunneling between two different dynamical states, namely clockwise and counterclockwise propagating waves. Since these two coupled waves occupy the same spatial domain, we can find an analogy with dynamical tunneling [7,8], in contrast to a conventional tunneling between spatially separate domains. The bistable transition of such a WGM doublet has already been experimentally observed [15,16].

For a conventional resonant tunneling which occurs between spatially separate regions, it is well known that a cubic nonlinearity such as the Kerr nonlinearity can suppress the tunneling rate. For instance, if the population of two spatially separate symmetric potential wells are unevenly excited, the excited population can break the symmetry of the system through the nonlinearity and leads to the suppression of the resonant tunneling between the separate wells. Such effects of the cubic nonlinearity are referred to as "self-trapping." Since the cubic nonlinearity appears in the nonlinear Schrödinger equation, i.e., the governing equation of a bosonic many-body system by mean-field approximation, such self-trapping processes have been well studied in Bose-Einstein condensates [17]. Recently, the effect of the cubic nonlinearity has also

been investigated by using WGMs in microcavities [18,19]. In particular, Ref. [18] shows that coupled WGMs of two or more microcavities can exhibit self-trapping, if the microcavities have a Kerr nonlinearity.

Contrary to Ref. [18], we address the effect of the cubic nonlinearity on the dynamical tunneling by using the doublet of a WGM. In this work, the two modes of a WGM doublet are coupled in a single microcavity by perturbing the evanescent field. Because the coupled modes are excited in the same mode volume, the change of the refractive index by the Kerr nonlinearity affects both of the modes in the same way. Therefore, different effects of the Kerr nonlinearity are expected, compared to those occurring for the conventional tunneling.

With this motivation, we investigate how the Kerr nonlinearity affects the doublet of WGMs, using numerical and theoretical models. As a model system, we choose an "add-drop filter" [20–29], which is comprised of a microcavity and two waveguides coupled to the cavity. Using this system, we can pick up a certain component from the incoming wave in one waveguide, which is resonant to a WGM of the microcavity, and redirect it to the other guide. This feature of the add-drop filter is valuable because it can be applied to channel dropping. Therefore, the add-drop filters have been experimentally realized with diverse test bathes, including photonic crystals and silica microspheres [21–23]. Also various aspects of this device has been investigated numerically and theoretically [24–29].

In this work, the transmission and the mode dynamics of the add-drop filter are numerically and theoretically analyzed, varying the Kerr nonlinearity of the microcavity. In the numerical simulation of the add-drop filter, it is observed that one directional whispering gallery mode becomes dominant when the Kerr nonlinearity is increased. The reason behind this is mainly that the perturbation that lifts the degeneracy between the states also leads to uneven linewidths of the doublet, and they result in different bistable transitions. Using the theoretical model based on "coupled-mode theory (CMT)" [20,28,29], we analyze the details of the mode dynamics behind the phenomena. The theoretical model of CMT has also been proven to be applicable to the optical frequency comb experiments [30].

In the next section, the add-drop filter will be introduced, and the numerical simulation of its transmission and WGM doublets will be presented. In Sec. III, the effect of the nonlinearity on the transmission and the WGMs will be investigated. To analyze the properties of the mode dynamics, such as the rotation and the stability of WGMs, a theoretical model will be built on the basis of CMT [20,28,29]. By analyzing the mode dynamics, the physical background behind the observed phenomena will be clarified. The results of the numerical simulations in this work will first be presented with nondimensionalized units. Then, the experimental realizability of our work will be discussed with the realistic units at the end of Sec. III.

II. ADD-DROP FILTER AND CMT MODELING

The add-drop filter consists of a microcavity and two optical fibers that are side coupled to the cavity through an evanescent field. The two waveguides effectively provide four channels. In Fig. 1, the four channels are indexed by $i = 1, 2, 3$, and 4. In this work, the field in the lower waveguide is not analyzed. However, we keep it in the scheme for two reasons. First, the lower waveguide makes the geometry of the system twofold symmetric, which helps lift the degeneracy of WGMs more easily. Second, if the waveguide which has the incoming wave is not experimentally available for the measurement of the outgoing wave, the mode dynamics presented in this work can be investigated by measuring the outgoing wave in the lower waveguide.

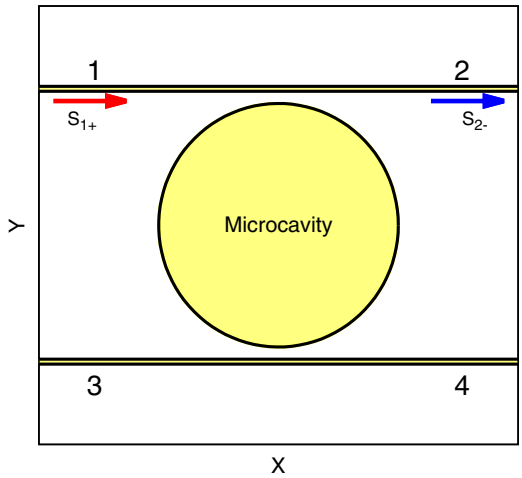

FIG. 1. Structure of the add-drop filter: a circular microcavity with radius R is coupled to two waveguides. The four branches given by the waveguides are indexed by $i = 1, 2, 3$, and 4. The coupling is through the scattering of evanescent fields on the waveguides. The width of the waveguides is $0.04R$ and the closest gap between the cavity and the waveguides is $0.1R$. The transmission from channel 1 to channel 2 are numerically computed by the ratio of the outgoing wave S_{2-} to the incoming wave S_{1+}.

In this add-drop filter, the shortest distance between the cavity boundary and the waveguide is set equal to $0.1R$, where R is the radius of the cavity. The refractive index of the cavity and the waveguide is chosen to be $n_0 = 2.0$. In order to induce a strong backscattering of evanescent field and to thereby lift the degeneracy of a WGM more easily, very narrow waveguides with the width of $0.04R$ are put at the upper and lower sides of the cavity. To investigate the transmission, a continuous-wave source with frequency Ω is set at channel 1, which provides the incoming wave S_{1+}. In the numerical analysis, the amplitude of the source S_{1+} is set equal to 10, and the wave arriving in channel 2, S_{2-}, is computed by means of the finite-difference time domain (FDTD) method [31,32]. The numerical computation is first performed with the units of length and time that are scaled by $0.2R$ and $0.2R/c$, respectively, where c is the speed of light.

If a mode with an extremely high cavity-Q factor is excited in the microcavity, the coupling via scattering can lift the intrinsic degeneracy of the doublet state and split the modes [4,14]. The scattering on the two waveguides attached to the cavity is adjusted to be strong enough to lift the degeneracy. By the FDTD simulation, such a coupling is observed. Figure 2 shows that a whispering gallery mode with

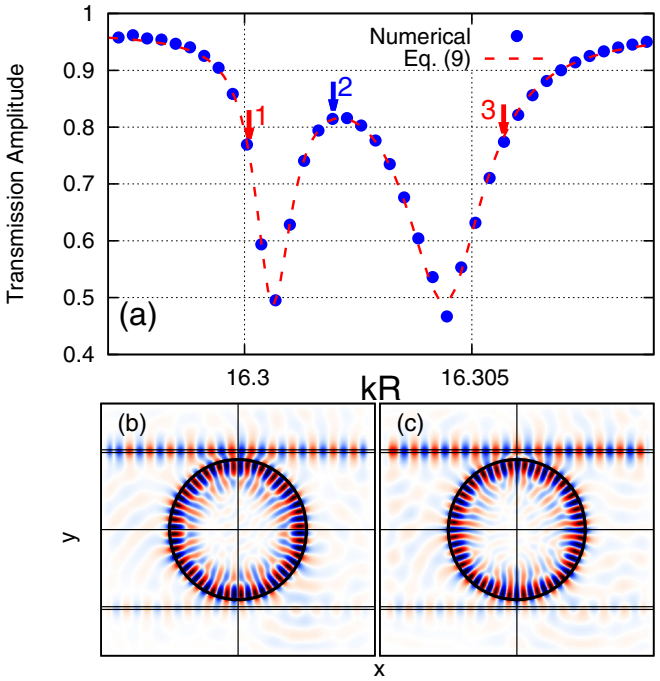

FIG. 2. (a) Transmission amplitude at channel 2 without Kerr nonlinearity. Due to the scattering on the waveguides and the high Q factor of the resonance, the transmission dip is split. The excited waves in the cavity on the left-hand side and the right-hand side of the split dips (denoted by 1 and 3) exhibit clockwise rotation, whereas the wave between the split dips (denoted by 2) shows counterclockwise rotation. The result of the comparison with Eq. (9) is superimposed as a dotted curve. Each dip exhibits different parity [(b) odd, (c) even] with respect to the symmetry axes of the system.

the radial mode number $l = 1$ and the azimuthal mode number $m = 28$ is coupled to the waveguide. As the cavity modes have extremely high Q factors, the transmission curve exhibits two split dips, and each dip corresponds to a different parity with respect to the reflectional symmetric axis. In Fig. 2(a), it is noted that the transmission amplitude of each dip reaches 0.5. This implies that this device transfers 25% of the incoming flux from the upper waveguide to the lower as a channel-dropping filter. Figures 2(b) and 2(c) show the two modes corresponding to the left and the right dips in the transmission curve in Fig. 2(a), which display odd and even symmetry, respectively.

Another noteworthy feature can be found in the rotation of the excited wave, which depends on the relative position to the split peaks. As the incoming wave runs from the left-hand side to the right-hand side of the upper waveguide in Fig. 1, it is intuitively expected that the wave in the cavity would be launched on the upper side of the cavity parallel to the incoming wave, and thus the excited field in the cavity would rotate in the clockwise direction. However, they exhibit the counterclockwise field rotation in between the split dips, contrary to the intuitive expectation, whereas on the right-hand and the left-hand sides of the split dips, they show the more intuitive clockwise rotation [14].

The splitting of the WGMs is analyzed by using "coupled-mode theory." For the sake of intuitive modeling, two counter-rotating modes with the same resonant frequency ω are initially adopted as a basis, and the following equations are derived:

$$\frac{da_c}{dt} = \left[i(\omega+g) - \gamma - \tfrac{1}{2}\Gamma\right]a_c + \left(ig - \tfrac{1}{2}\Gamma\right)a_{cc} + \eta_c S_{1+}, \tag{1}$$

$$\frac{da_{cc}}{dt} = \left[i(\omega+g) - \gamma - \frac{1}{2}\Gamma\right]a_{cc} + \left(ig - \frac{1}{2}\Gamma\right)a_c + \eta_{cc} S_{1+}. \tag{2}$$

Here the subscripts c and cc stand for clockwise and counterclockwise modes, and g is the coupling parameter given by the scattering. γ is the characteristic attenuation of the WGM, given by the mode configuration [33,34], and Γ is the additional attenuation induced by the scattering. Although the source is put only in channel 1, it is necessary to assume the driving η_{cc} because the counterclockwise mode is also driven by scattering on the waveguides.

Since the modes associated with the two transmission dips are two standing-wave modes, the basis is transformed to

$$\psi_+ = \frac{\psi_c + \psi_{cc}}{2} \quad \text{and} \quad \psi_- = \frac{\psi_c - \psi_{cc}}{2i}. \tag{3}$$

For the circular microcavity, these modes are represented by the product of a Bessel function J_m and a sin or cos function, as follows:

$$\begin{aligned} \psi_+(r,\theta) &= J_m(nkr)\cos(m\theta), \\ \psi_-(r,\theta) &= J_m(nkr)\sin(m\theta), \end{aligned} \tag{4}$$

where n is the refractive index of the cavity and the waveguide, and k is the resonant wave number of the microcavity with the azimuthal mode number m. The resonant wave number is determined by solving Maxwell equations with the given microcavity boundary and mode numbers. Corresponding to the change of basis, the mode equations in Eqs. (1) and (2) are also rearranged in the form

$$\frac{da_+}{dt} = [i(\omega+2g) - \gamma - \Gamma]a_+ + \eta_+ S_{1+}, \tag{5}$$

$$\frac{da_-}{dt} = (i\omega - \gamma)a_- + \eta_- S_{1+}, \tag{6}$$

where the driving strengths are given by

$$\eta_+ = \frac{\eta_c + \eta_{cc}}{2} \quad \text{and} \quad \eta_- = \frac{\eta_c - \eta_{cc}}{2i}. \tag{7}$$

Then, the transmission amplitude at channel 2 can be formulated as

$$t = 1 - \frac{\eta_+^* a_+}{S_{1+}} - \frac{\eta_-^* a_-}{S_{1+}} \tag{8}$$

$$= 1 - \frac{|\eta_+|^2}{i(\omega+2g-\Omega) - \gamma - \Gamma} - \frac{|\eta_-|^2}{i(\omega-\Omega) - \gamma}. \tag{9}$$

Because some parameters in Eq. (9) cannot be analytically evaluated, the values of the couplings and attenuations are obtained by taking them as free parameters and comparing Eq. (9) with the numerical result from the FDTD simulation

in Fig. 2. This yields

$$|\eta_+|^2 = 5.043 \times 10^{-5}, \quad |\eta_-|^2 = 1.159 \times 10^{-4},$$
$$\gamma = 1.118 \times 10^{-4}, \quad \Gamma = 1.135 \times 10^{-4}. \tag{10}$$

To obtain these values, the contributions of the neighboring modes to the transmission are carefully considered. In the spectrum of a circular microcavity, the $(m,l) = (20,3)$ and the (24,2) modes (m: azimuthal mode number; l: radial mode number) are standing on the left-hand and the right-hand sides of the doublet, respectively. Their contributions to the transmission are extracted prior to the comparison.

With the values in Eq. (10), Q factors of the spilt modes can be computed by

$$Q_+ = \frac{\omega + 2g}{2(\Gamma + \gamma)}, \quad Q_- = \frac{\omega}{2\gamma}, \tag{11}$$

which yields the order of 10^5. These computed Q factors are lower, by a factor of 10^{-3}, than the experimentally available values, which can be of the order of 10^8 [2,3]. This is mainly attributed to the low wave numbers kR that are considered in the computation. Due to computational limitation concerning the number of lattice grid points and time steps that we can account for in the numerical simulation, the computed modes have smaller wave numbers as well as smaller mode numbers than WGMs in experiments. This leads to a larger geometrical damping and a higher coupling with the waveguide modes, which inevitably results in such low Q factors.

III. KERR NONLINEARITY IN NUMERICAL COMPUTATION AND CMT MODELING

In a Kerr medium, the electric field and the electric displacement are related by the nonlinear equation [1]

$$\mathbf{D} = \epsilon_0(1 + \chi^{(0)})\mathbf{E} + \epsilon_0\chi^{(3)}\mathbf{E}^3. \tag{12}$$

By substituting a monochromatic electromagnetic wave $\mathbf{E} = \mathbf{E}_\omega \exp(i\omega t)$ into Eq. (12), the third-order nonlinear term in Eq. (12) leads to

$$[\mathrm{Re}(\mathbf{E}_\omega e^{-i\omega t})]^3 = \frac{1}{4}\mathrm{Re}\left(\mathbf{E}_\omega^3 e^{-3i\omega t}\right) + \frac{3}{4}|\mathbf{E}_\omega|^2\mathrm{Re}(\mathbf{E}_\omega e^{-i\omega t}). \tag{13}$$

By neglecting the third-harmonic term, the effective refractive index can be written in the well-known form

$$n = n_0 + \frac{3\chi^{(3)}}{4n_0^2}|\mathbf{E}|^2. \tag{14}$$

The effect of the Kerr nonlinearity on the split whispering gallery modes is first numerically investigated. In this simulation, the pumping power is set equal to $|S_{1+}|^2 = 100$ and the unit of $\chi^{(3)}$ is accordingly scaled. Figure 3 presents the FDTD computation of the transmission amplitude through the add-drop filter and its evolution with the increase of $\chi^{(3)}$. As the nonlinearity increases, the resonance profiles in the transmission curves lean more toward the left-hand side. When the nonlinearity exceeds a certain value, it is noticed that an abrupt upward shift occurs in both of the transmission dips. This is an evidence of the bistable transition because unstable

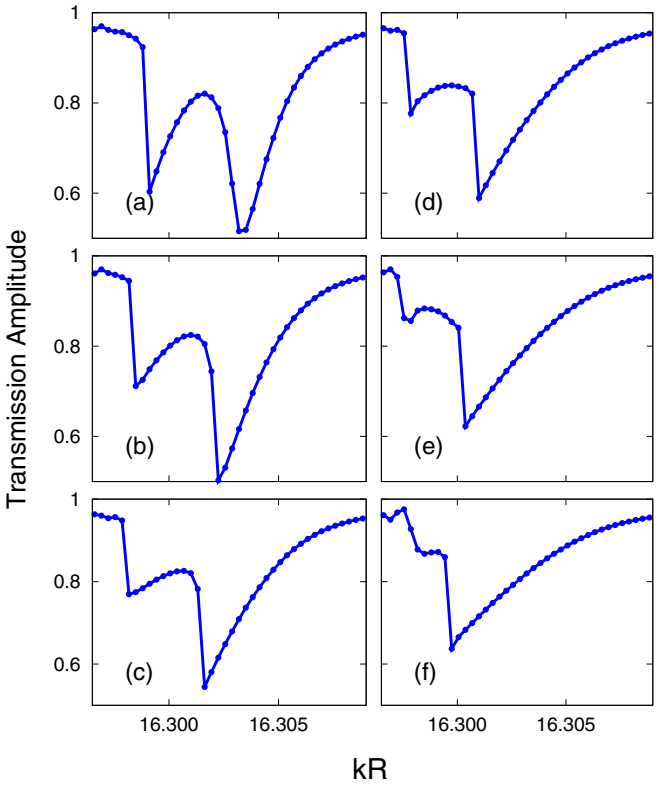

FIG. 3. FDTD simulation of the transmission amplitude associated with the split whispering gallery modes. (a) $\chi^{(3)} = 1.0 \times 10^{-7}$, (b) 2.0×10^{-7}, (c) 3.0×10^{-7}, (d) 4.0×10^{-7}, (e) 5.0×10^{-7}, and (f) 6.0×10^{-7}. The intensity of the whispering gallery modes lies in the range of $|\mathbf{E}|^2 = 2 \sim 6 \times 10^4$.

mode dynamics is involved in the parts where the abrupt shifts occur.

The bistable transition progresses gradually with the increase of $\chi^{(3)}$. The remarkable feature in this transition is the difference in the bistable transition of the two dips. Namely, the broader a dip is, the slower it goes bistable with increase of the nonlinearity. For instance, at $\chi^{(3)} = 1.0 \times 10^{-7}$, the left-hand-side dip shows the bistability, whereas the right-hand-side dip does not yet. Obviously, this difference results from the uneven linewidth of the doublet. As seen in the previous section, the two dips of the doublet states have different damping rates in the linear regime, which are given by γ and $\Gamma + \gamma$, respectively, for the right- and the left-hand-side dips. This uneven transition to bistability leads to two uneven depths of the dips in the transmission profile, as shown in Fig. 3. Another noticeable observation in this computation is that the clockwise rotation of the field gets dominant when the value of $\chi^{(3)}$ is sufficiently large, such as 5×10^{-7}. As the transmission dips lean to the left-hand side, the spectral region between the two dips which shows the counterclockwise field rotation shrinks, and the transmission dip on the left-hand side vanishes. In contrast, the right-hand-side curve of the dip remains and keeps the clockwise field rotation as it has in the linear optical regime.

Using the CMT model, this numerical observation can be reconstructed and the underlying mode dynamics behind the observation can be addressed more clearly. To apply the

CMT model to the system, the Kerr-nonlinear effect can be incorporated in the model by treating it as a perturbation. For other values necessary for the model, such as attenuations and resonant frequencies, those in Eq. (10) are used. The electric field in the cavity has to be first represented with the basis functions, $\boldsymbol{\psi}_+$ and $\boldsymbol{\psi}_-$, as follows:

$$\mathbf{E} = a_+(t)\boldsymbol{\psi}_+(\mathbf{r}) + ia_-(t)\boldsymbol{\psi}_-(\mathbf{r}), \tag{15}$$

where an imaginary number i is multiplied to the term of ψ_- to reveal both the relationship to the rotational basis more explicitly and consistency with Eq. (3). Then, the field intensity formed in the cavity is proportional to

$$|\mathbf{E}|^2 = (a_+^*\boldsymbol{\psi}_+ - ia_-^*\boldsymbol{\psi}_-)(a_+\boldsymbol{\psi}_+ + ia_-\boldsymbol{\psi}_-). \tag{16}$$

By applying the perturbation approach to Eq. (14) [35], the mode equations in Eqs. (5) and (6) are modified to

$$\frac{da_+}{dt} = [i(\omega+2g) - \gamma - \Gamma]a_+ + i\omega\kappa_{++}|a_+|^2a_+ + i\omega\kappa_{+-}(2a_+|a_-|^2 - a_+^*a_-^2) + \eta_+S_{1+}, \tag{17}$$

$$\frac{da_-}{dt} = (i\omega - \gamma)a_- + i\omega\kappa_{--}|a_-|^2a_- + i\omega\kappa_{+-}(2a_-|a_+|^2 - a_-^*a_+^2) + \eta_-S_{1+}, \tag{18}$$

where κ_{++},κ_{+-} and κ_{--} are given by

$$\kappa_{pq} = \frac{3\chi^{(3)}}{4n^2}\frac{\int|\psi_p|^2|\psi_q|^2dV}{\int|\psi_+|^2+|\psi_-|^2dV}, \quad \text{where } p,q = + \text{ or } -. \tag{19}$$

The integral in Eq. (19) is conducted for the area of the microcavity. If the standing wave modes in Eq. (4) are substituted into the above equation, the κ's are related by

$$\kappa_{++} = \kappa_{--} = 3\kappa_{+-}. \tag{20}$$

Due to the overlapped mode volume of dynamical tunneling, κ_{+-} is considerably large in comparison to a system involving a spatial tunneling, such as two microcavities coupled through evanescent field overlap.

In order to search for stationary states of the mode equations, the following Ansätze are first introduced:

$$a_+ = A_+e^{i(\Omega t+\phi_+)}, \tag{21}$$

$$a_- = A_-e^{i(\Omega t+\phi_-)}. \tag{22}$$

By substituting Eqs. (21) and (22) into Eqs. (17) and (18), the mode equations are reduced to

$$i\Omega A_+ = [i(\omega+2g) - \gamma - \Gamma]A_+ + i3\omega\kappa A_+^3 + i\omega\kappa[2A_+A_-^2 - A_+A_-^2e^{-i2(\phi_+-\phi_-)}] + K_+e^{-i\phi_+}, \tag{23}$$

$$i\Omega A_- = (i\omega - \gamma)A_- + i3\omega\kappa A_-^3 + i\omega\kappa[2A_-A_+^2 - A_-A_+^2e^{i2(\phi_+-\phi_-)}] - iK_-e^{-i\phi_-}, \tag{24}$$

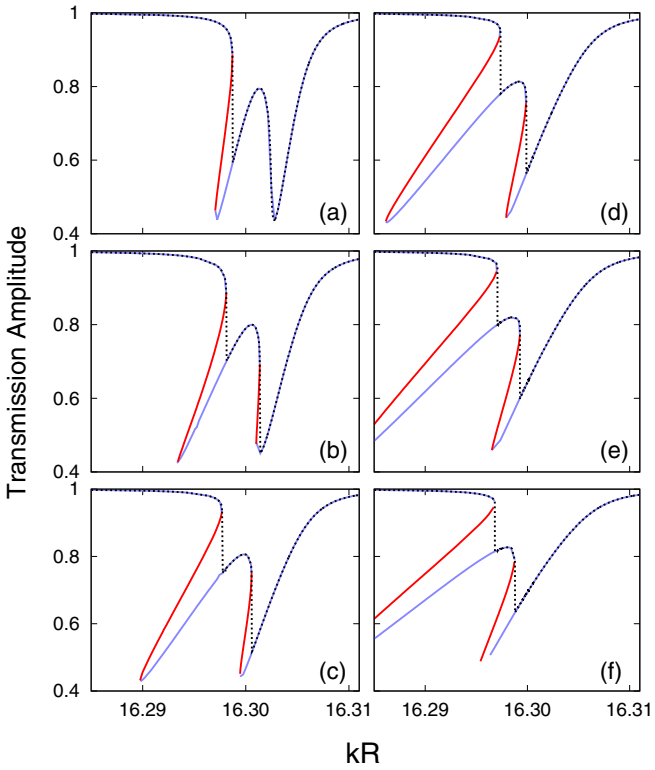

FIG. 4. Results of the CMT analysis for the split transmission under $\chi^{(3)}$ nonlinearity. With increasing nonlinearity, stationary states are identified and plotted. Stable and unstable branches of the profile are denoted by blue and red colors, respectively. (a) $\chi^{(3)} = 1.0\times10^{-7}$, (b) 2.0×10^{-7}, (c) 3.0×10^{-7}, (d) 4.0×10^{-7}, (e) 5.0×10^{-7}, and (f) 6.0×10^{-7}. The superimposed black dotted lines are connecting the branches that are most likely to be observed in numerics and in an experiment. They show good agreement with Fig. 3.

where $K_\pm$ are given by $|\eta_\pm|K$ and the amplitude K of the source is set equal to 10, as the source amplitude in the numerical computation.

By numerically determining self-consistent solutions of Eqs. (23) and (24), stationary states are identified at a given nonlinearity κ and a driving frequency. To facilitate the comparison with the full numerical solution, the obtained stationary states are converted to transmission amplitude by using Eq. (8). The result of the computation reveals the underlying bistability profile of the full numerical solution. Figure 4 shows a bistable transition in the transmission profiles, following the increase of nonlinearity.

As mentioned in Sec. I, when the $\chi^{(3)}$ nonlinearity exceeds a certain threshold, three stationary states correspond to one frequency in a bistable range. In this case, the two states with the highest and the lowest amplitudes have stable mode dynamics around themselves, whereas the one in the middle has unstable dynamics.

As the resonance profile is tilted by the bistable transition, there arises naturally a possibility that the profile can have an overlap with the nearest mode on the leaning side of the bistability. For the WGM doublet under the investigation, the nearest mode on the leaning side of the bistability, i.e.,

the left-hand side on the spectrum, is the mode with the mode numbers $(l,m) = (20,3)$, and its resonant wave number is given by $kR = 16.225$. Figure 5 shows that this neighboring mode is still far away from the WGM mode under consideration, compared to the width and the tilt of the leaning peaks. The latter is determined by

$$\delta kR = \kappa kR \mathrm{Re}[3A_-^2 + A_+^2(1 - e^{i(\phi_+ - \phi_-)})]. \quad (25)$$

Thus, the possibility of a coupling to this mode can be neglected.

In order to measure the stability of stationary states, Ansätze are introduced for a_+ and a_-:

$$a_+ = (\alpha_+ + i\beta_+)e^{i\Omega t} \text{ and } a_- = (\alpha_- + i\beta_-)e^{i\Omega t}, \quad (26)$$

where the real and the imaginary parts of the complex amplitudes α and β are time dependent, unlike A_+ and A_- in Eqs. (21) and (22).

By substituting a_+ and a_- in Eq. (26) into Eqs. (17) and (18) and by separating the real and the imaginary parts, the following four coupled equations are derived:

$$\begin{aligned}
\frac{d\alpha_+}{dt} &= -(\gamma + \Gamma)\alpha_+ - (\omega + 2g - \Omega)\beta_+ - 3\omega\kappa(\alpha_+^2 + \beta_+^2)\beta_+ - 2\omega\kappa(\alpha_-^2 + \beta_-^2)\beta_+ + \kappa\omega(2\alpha_-\beta_-\alpha_+ - \alpha_-^2\beta_+ + \beta_-^2\beta_+) + K_+,\\
\frac{d\beta_+}{dt} &= (\omega + 2g - \Omega)\alpha_+ - (\gamma + \Gamma)\beta_+ + 3\omega\kappa(\alpha_+^2 + \beta_+^2)\alpha_+ + 2\omega\kappa(\alpha_-^2 + \beta_-^2)\alpha_+ + \kappa\omega(\alpha_+\beta_-^2 - \alpha_+\alpha_-^2 - 2\alpha_-\beta_-\beta_+),\\
\frac{d\alpha_-}{dt} &= -\gamma\alpha_- - (\omega - \Omega)\beta_- - 3\omega\kappa(\alpha_-^2 + \beta_-^2)\beta_- - 2\omega\kappa(\alpha_+^2 + \beta_+^2)\beta_- + \kappa\omega(2\alpha_+\beta_+\alpha_- - \alpha_+^2\beta_- + \beta_+^2\beta_-),\\
\frac{d\beta_-}{dt} &= (\omega - \Omega)\alpha_- - \gamma\beta_- + 3\omega\kappa(\alpha_-^2 + \beta_-^2)\alpha_- + 2\omega\kappa(\alpha_+^2 + \beta_+^2)\alpha_- + \kappa\omega(\alpha_-\beta_+^2 - \alpha_-\alpha_+^2 - 2\alpha_+\beta_+\beta_-) - K_-. \quad (27)
\end{aligned}$$

The stability at given amplitudes can be inferred from the Jacobian matrix of the above four equations. If the eigenvalues of the Jacobian matrix are all negative, the associated stationary state has a stable mode dynamics around it, while an unstable dynamics is inferred otherwise [36–38]. The result of the stability computation is encoded on the resonance profile with a color code. In Fig. 4, stable and unstable branches are denoted by blue and red colors, respectively.

If the stability of a stable branch is quantified by the smallest absolute value of the eigenvalues of the Jacobian matrix, the higher stable branch in the transmission curve has a larger stability that the lower one. Therefore, the upper branch is more likely to be numerically converged and experimentally observed. In Fig. 4, the curves connecting upper stable branches are superimposed as black dotted lines. These curves show a good agreement with the numerical results in Fig. 3.

In this computation, the difference in the bistable transition of the two dips is also observed. As seen in Fig. 3, the right-hand-side dip in Fig. 4 is still completely monostable at $\chi^{(3)} = 1 \times 10^{-7}$, whereas the left-hand-side dip already gets into the bistable regime. This is apparently caused by the uneven damping of the doublet. Since the two dips have different dampings, namely γ and $\gamma + \Gamma$ in the linear regime, the right-hand-side dip with higher damping shows slower bistable transition. In the end, the right-hand-side dip takes up the most part of the dotted curve in Fig. 4, whereas the left-hand-side dip is strongly suppressed when it goes to the bistable regime. At the same time, the spectral region between the two dips which shows the counterclockwise field rotation, shrinks. In the bistable transition, each part of the transmission dip keeps the field rotation. Hence, WGMs dominantly show a clockwise rotation over the transmission dips when the system gets into the strongly bistable regime.

To more clearly render the mode dynamics behind this phenomenon, the associated rotating amplitudes are reconstructed by CMT modeling, again. For this purpose, the basis functions are transformed back to the rotational basis by reversing Eq. (3). Figure 5 shows the result of the transformation. In Fig. 5, the amplitude of the clockwise rotating mode is displayed by a dotted curve, and that of the counterclockwise rotating one is represented by a solid curve. In the bistable transition, one of these curves exhibits a twist of the peak, whereas the other one shows a leaning peak to the left-hand side. By comparing the amplitude of the clockwise and the counterclockwise modes, the part of the curve where the counterclockwise rotation is dominant is identified and shaded with gray color in Fig. 5. In this comparison, the amplitude in the lower stable branch is chosen in the bistable region because the lower branch has the higher stability. The figure shows an apparent tendency, namely that the region of the counterclockwise rotation shrinks with the increase of nonlinearity. In other words, the clockwise becomes dominant over the resonant profile, as is also numerically observed.

Let us finally discuss the relevance of this work to practical experiments. If the model system is experimentally incorporated by a silicon-dioxide microcavity with a diameter of 100 μm and the intracavity intensity of 1 GW cm^{-2} is induced, the investigated range of $\chi^{(3)}$ corresponds to

$$\chi^{(3)} = 5 \sim 15 \times 10^{-16} \text{ cm}^2/\text{W}. \quad (28)$$

The $\chi^{(3)}$ value of a silicon-dioxide material lies in the lower part of this range.

The magnitude of the pumping power in the simulation can be obtained by the squared amplitude S_{1+} in Eqs. (1) and (2) with the same scaling for the magnitude of $\chi^{(3)}$. This yields the intensity of 10^3 W, which is much higher than the pumping power in experiments [2,3]. However, this discrepancy can be justified by the large leakage of the WGM in the simulation. As the WGMs in our simulation have smaller wave numbers and

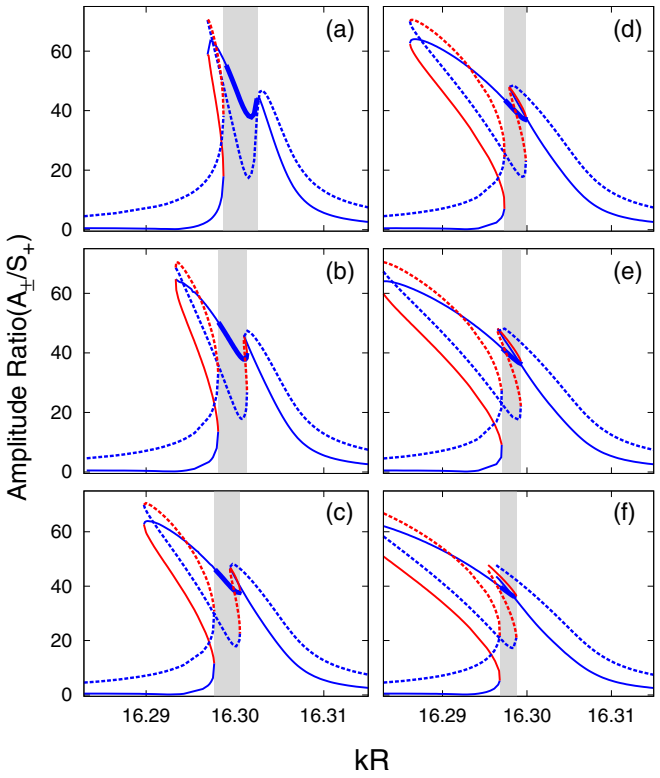

FIG. 5. Relative amplitudes of clockwise (dotted line) and counterclockwise (solid line) rotating modes with respect to the driving amplitude S_+. The stability of each branch is denoted by the same color code as in Fig. 4 (stable: blue; unstable: red). (a) $\chi^{(3)} = 1.0 \times 10^{-7}$, (b) 2.0×10^{-7}, (c) 3.0×10^{-7}, (d) 4.0×10^{-7}, (e) 5.0×10^{-7}, and (f) 6.0×10^{-7}. The range where the counterclockwise rotating mode is dominant is shaded by gray color, and the corresponding amplitude that is likely dominant in this range is denoted by a thick line.

lower Q factors than those in experiments, the leakage of the mode intensity is inevitably higher. In order to compensate for such a high leakage and induce the intracavity intensity which is comparable to the experimental value and high enough for the Kerr effect, it is necessary to assume a high enough pumping power.

As the CMT model is verified by the good agreement with the FDTD simulation, our theoretical model is applied to realistic values of wave numbers with a practical pumping power, such that $nkR \sim 100$ with 0.1 W for pumping. For the mode damping γ and Γ, values are chosen of the order of 10^{-8}, where the values deduced from experimental Q factors of WGMs lie. As Fig. 6 shows, the result confirms the same behavior of the split resonance, i.e., that one rotational wave gets dominant in a doublet with increase of the Kerr nonlinearity. Since the bistable transition of a WGM doublet under Kerr nonlinearity have been experimentally observed [15,16] and, in particular, it is shown that the symmetry breaking can occur at powers below the threshold for frequency comb generation [16], the underlying mode dynamics presented in this work can also be experimentally verified and the result of this study can be applied to frequency comb generation.

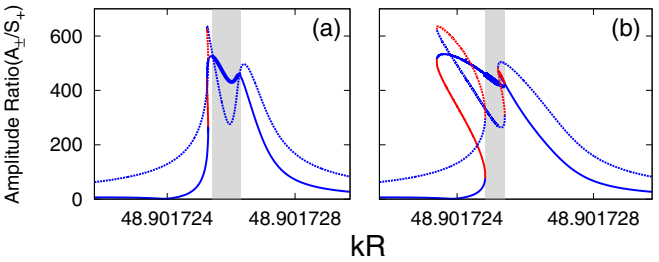

FIG. 6. The same computation as in Fig. 5 with practical parameters. For this computation, we set $\omega = 48.901725$ and $g = 4.63 \times 10^{-7}$ with 0.1 W for pumping. For each mode, dampings are set equal to $\gamma = 4.22 \times 10^{-8}$ and $\Gamma = 3.38 \times 10^{-8}$. As the Kerr nonlinearity increases from (a) $\chi^{(3)} = 1.0 \times 10^{-7}$ to (b) 5.0×10^{-7}, the spectral range where the counterclockwise mode is dominant (shaded by gray color) reduces.

IV. CONCLUSION

The effect of a Kerr nonlinearity on coupled whispering gallery modes is investigated numerically and theoretically. In this study, an optical add-drop filter, which consists of a microcavity and two side-coupled waveguides, is chosen as a model system. When a whispering gallery mode with extremely high Q factor is induced in the microcavity, the intrinsic degeneracy of the whispering gallery mode can be lifted by scattering of the evanescent field, thus forming a doublet state. Correspondingly, the transmission curve also exhibits two split downward peaks. The evolution of these split peaks with increasing nonlinearity is first numerically investigated by using the FDTD algorithm. In this computation, the transmission shows a typical bistable transition under the influence of the cubic nonlinearity. However, the two peaks of the doublet show different transition to bistability, since the two peaks have different dampings. As a result, one side of the peak with higher damping takes a large part of the transmission curve as soon as the bistability is induced. Thus, the rotation of field that is mainly observed on this side of the peak gets dominant.

These numerically observed phenomena are addressed by a coupled-mode-theory (CMT) model. Using the perturbation approach, we incorporate the nonlinear optical effect in the CMT model and obtain the dynamics of modes in the microcavity. This theoretical modeling shows a quantitative consistency with the numerical observations and reveals how the one-directional rotation of field becomes dominant with increasing nonlinearity.

Using the theoretical analysis developed in this work, we anticipate that the various experiments which exhibit cubic-nonlinear phenomena in a microcavity, such as optical circuits and optical frequency comb generators, can be addressed.

ACKNOWLEDGMENT

This work is financially supported by Deutsche Forschungsgemeinschaft (DFG) within the framework of Forschergruppe FOR760.

[1] R. W. Boyd, *Nonlinear Optics*, 3rd ed. (Academic, New York, 2008).

[2] P. Del'Haye, A. Schliesser, O. Arcizet, T. Wilken, R. Holzwarth, and T. J. Kippenberg, Nature (London) **450**, 1214 (2007).

[3] P. Del'Haye, O. Arcizet, A. Schliesser, R. Holzwarth, and T. J. Kippenberg, Phys. Rev. Lett. **101**, 053903 (2008).

[4] T. J. Kippenberg, S. M. Spillane, and K. J. Vahala, Opt. Lett. **27**, 1669 (2002).

[5] A. Rodriguez, M. Soljacic, J. D. Joannopoulos, and S. G. Johnson, Opt. Express **15**, 7303 (2007).

[6] *Dynamical Tunneling: Theory and Experiment*, edited by S. Keshavamurthy and P. Schlagheck (CRC, Boca Raton, FL, 2011).

[7] M. J. Davis and E. J. Heller, J. Chem. Phys. **75**, 246 (1981).

[8] C. Dembowski, H.-D. Gräf, A. Heine, R. Hofferbert, H. Rehfeld, and A. Richter, Phys. Rev. Lett. **84**, 867 (2000).

[9] H. Kwak, Y. Shin, S. Moon, S.-B. Lee, J. Yang, and K. An, Sci. Rep. **5**, 9010 (2015).

[10] J. Yang, S.-B. Lee, S. Moon, S.-Y. Lee, S. W. Kim, Truong Thi Anh Dao, J.-H. Lee, and K. An, Phys. Rev. Lett. **104**, 243601 (2010).

[11] S. Gehler, S. Löck, S. Shinohara, A. Bäcker, R. Ketzmerick, U. Kuhl, and H.-J. Stöckmann, Phys. Rev. Lett. **115**, 104101 (2015).

[12] W. K. Hensinger, H. Haffner, A. Browaeys, N. R. Heckenberg, K. Helmerson, C. McKenzie, G. J. Milburn, W. D. Phillips, S. L. Rolston, H. Rubinsztein-Dunlop, and B. Upcroft, Nature (London) **412**, 52 (2001).

[13] D. A. Steck, W. H. Oskay, and M. G. Raizen, Science **293**, 274 (2001).

[14] A. Mazzei, S. Götzinger, L. de S. Menezes, G. Zumofen, O. Benson, and V. Sandoghdar, Phys. Rev. Lett. **99**, 173603 (2007).

[15] F. Treussart, V. S. Ilchenko, J.-F. Roch, J. Hare, V. Lefevre-Seguin, J.-M. Raimond, and S. Haroche, Eur. Phys. J. D **1**, 235 (1998).

[16] L. Del Bino, J. M. Silver, S. L. Stebbings, and P. Del'Haye, arXiv:1607.01194.

[17] A. Smerzi, S. Fantoni, S. Giovanazzi, and S. R. Shenoy, Phys. Rev. Lett. **79**, 4950 (1997); M. Albiez, R. Gati, J. Fölling, S. Hunsmann, M. Cristiani, and M. K. Oberthaler, *ibid.* **95**, 010402 (2005).

[18] H. Ramezani, T. Kottos, V. Shuvayev, and L. Deych, Phys. Rev. A **83**, 053839 (2011).

[19] E. Bulgakov, K. Pichugin, and A. Sadreev, J. Phys: Condens. Matter **25**, 395304 (2013).

[20] C. Manolatou, M. J. Khan, S. Fan, P. R. Villeneuve, H. A. Haus, and J. D. Joannopoulos, IEEE J. Quantum Electron. **35**, 1322 (1999).

[21] F. Monifi, J. Friedlein, S. K. Ozdemir, and L. Yang, J. Lightwave Technol. **30**, 3306 (2012).

[22] M. L. Gorodetsky, A. A. Savchenkov, and V. S. Ilchenko, Opt. Lett. **21**, 453 (1996).

[23] M. Cai, O. Painter, and K. J. Vahala, Phys. Rev. Lett. **85**, 74 (2000).

[24] Q. Chen, Y.-D. Yang, and Y.-Z. Huang, Appl. Phys. Lett. **89**, 061118 (2006).

[25] B. E. Little, S. T. Chu, H. A. Haus, J. Foresi, and J.-P. Laine, J. Lightwave Technol. **15**, 998 (1997).

[26] Z. Qiang, W. Zhou, and R. A. Soref, Opt. Express **15**, 1823 (2007).

[27] Q. Huang and J. Yu, Opt. Express **22**, 25171 (2014).

[28] P. Chak, S. Pereira, and J. E. Sipe, Phys. Rev. B **73**, 035105 (2006).

[29] E. F. Franchimon, K. R. Hiremath, R. Stoffer, and M. Hammer, J. Opt. Soc. Am. B **30**, 1048 (2013).

[30] Y. K. Chembo and N. Yu, Phys. Rev. A **82**, 033801 (2010).

[31] Allen Taflove and Susan C. Hagness, *Computational Electrodynamics: The Finite-Difference Time-Domain Method* (Artech, London, 2005).

[32] A. F. Oskooi, D. R. M. Ibanescu, P. Bermel, J. D. Joannopoulos, and S. G. Johnson, Comput. Phys. Commun. **181**, 687 (2010).

[33] J. Uwe Nöckel, Ph.D. thesis, Yale University, 1997.

[34] Jeong-Bo Shim and Jan Wiersig, Opt. Express **21**, 24240 (2013).

[35] V. Grigoriev and F. Biancalana, J. Opt. Soc. Am. B **28**, 2165 (2011).

[36] E. Ott, *Chaos in Dynamical Systems* (Cambridge University Press, London, 2002).

[37] N. M. Litchinitser, C. J. McKinstrie, C. Martijn de Sterke, and G. P. Agrawal, J. Opt. Soc. Am. B **18**, 45 (2001).

[38] A. R. Cowan and J. F. Young, Phys. Rev. E **68**, 046606 (2003).